Biomaterials Science

ROYAL SOCIETY OF CHEMISTRY

PAPER

View Article Online
View Journal | View Issue

Check for updates

Cite this: *Biomater. Sci.*, 2021, **9**, 5247

A neutrophil-mimetic magnetic nanoprobe for molecular magnetic resonance imaging of stroke-induced neuroinflammation†

Chunming Tang,‡ Qianqian Wang,‡ Kaiming Li, Xiuqi Li, Cong Wang, Lingjing Xue, Caoyun Ju* and Can Zhang *

Received 9th April 2021,
Accepted 26th May 2021

DOI: 10.1039/d1bm00566a

rsc.li/biomaterials-science

Neuroinflammation plays a key role in the progression of brain injury induced by stroke, and has become a promising target for therapeutic intervention for stroke. Monitoring this pivotal process of neuroinflammation is highly desirable to guide specific therapy. However, there is still a lack of a satisfactory nanoprobe to selectively monitor neuroinflammation. As endothelial cell activation is a hallmark of neuroinflammation, it would be clinically relevant to develop a non-invasive *in vivo* imaging technique to detect the endothelial activation process. Herein, inspired by the specific neutrophil–endothelium interaction, we designed neutrophil-camouflaged magnetic nanoprobes (NMNPs) that can be used to target activated endothelial cells for improved neuroinflammation imaging. NMNPs are composed of an inner core of superparamagnetic iron oxide (SPIO)-loaded poly(lactic-*co*-glycolic acid) (PLGA) nanoparticles and a biomimetic outer shell of a neutrophil membrane, which maintained the biocompatibility and targeting ability of neutrophils and the excellent contrast effects of SPIO. Moreover, we demonstrated that NMNPs can successfully bind to inflamed cerebral vasculature using the intravital imaging of live cerebral microvessels in transient middle cerebral artery occlusion (tMCAO) mice. After that, NMNPs could further accumulate in the brain vasculature and exhibit excellent contrast effects for stroke-induced neuroinflammation and biosafety. We believe that the neutrophil-camouflaged magnetic nanoprobe could serve as a highly safe and selective nanoprobe for neuroinflammation imaging and has alluring prospects for clinical application.

Introduction

Stroke is the second leading cause of death and a major cause of disability worldwide, resulting in approximately six million deaths annually. It can be classified as ischemic or hemorrhagic, and 85% of the cases are ischemic.[1,2] Among many detrimental cascades, neuroinflammation has come into the focus of research because of its key role in the progression of brain injury.[3–5] Although great advances have been made in experimental studies, transformation of the results of inflammatory modulating interventions into clinical settings is limited. Anti-inflammatory therapy in human stroke is restricted by the lack of sensitive and specific diagnosis to image the complex neuroinflammatory process.[6–8] Hence, imaging techniques that enable non-invasive, real-time detection of the neuroinflammatory process can significantly contribute to patient stratification, precision medicine and corresponding therapy from bench-to-bedside.

Magnetic resonance imaging (MRI) is an established versatile method for non-invasive imaging of ischemic stroke in clinical settings. In addition, recent developments in advanced MRI contrast agents that selectively target molecules involved in neuroinflammation offer the promise of *in vivo* molecular MRI of neuroinflammatory processes.[7,9–11] Therefore, the identification of specific molecular targets in neuroinflammation is highly attractive. Studies have shown that endothelial cell activation is the hallmark of neuroinflammation. Cerebral microvascular endothelial cells are swiftly activated after ischemic stroke and they subsequently upregulate a series of cell adhesion molecules (CAMs) including selectins, intercellular adhesion molecule (ICAM)-1 and vascular cell adhesion molecule (VCAM)-1. These CAMs are generally thought to be pro-inflammatory and thus detrimental in stroke-induced neuroinflammation. Hence, there is a growing acceptance of these CAMs as potential molecular MRI biomarkers.[12–14]

To this aim, a diverse array of targeted iron oxide particles conjugated with monoclonal antibodies against CAMs have

State Key Laboratory of Natural Medicines, Jiangsu Key Laboratory of Drug Discovery for Metabolic Diseases, Center of Advanced Pharmaceuticals and Biomaterials, China Pharmaceutical University, Nanjing, P.R. China.
E-mail: zhangcan@cpu.edu.cn, jucaoyun@cpu.edu.cn

†Electronic supplementary information (ESI) available. See DOI: 10.1039/d1bm00566a

‡These authors contributed equally to this work.

been successfully applied.[15,16] Although the established iron oxide platforms show efficient detection of stroke-induced neuroinflammation in animal models, several challenges still set a limitation to their clinical transformation. Firstly, these chemically modified iron oxide particles are easily recognized and cleared as exogenous substances by the reticuloendothelial system (RES). Secondly, despite a greater contrast effect with dual-targeted iron oxide particles, the optimizing molecular interactions between ligands and receptors by tuning the density and combination of targeting moieties are arduous to control. Thirdly, monoclonal antibodies decorated on iron oxide particles have potential immunogenicity which may lead to serious clinical consequences.[8,17–19] Thus, an ideal iron oxide particle based molecular MRI platform is expected to integrate biocompatibility, low immunogenicity and high binding affinity.

It is well documented that CAMs are markers of inflammation that promote leukocyte adhesion to activated vascular endothelium, especially by the neutrophil–endothelium interaction.[20] Neutrophils are generally the first and most abundant inflammatory cells to participate in the cerebral microvascular response upon ischemic stroke.[21] Hence, an ideal molecular MRI strategy should be able to mimic the behavior of neutrophils in terms of their ability to localize to the activated endothelial cells. The mimicking of neutrophils can be achieved by cloaking nanoparticles with natural neutrophil membranes.[22,23] These biomimetic nanoparticles inherit the collective biofunctions of the natural neutrophil membranes, such as biocompatibility, long circulation times, avoiding immunogenicity and high binding affinity to activated endothelial cells.[24] To our knowledge, the application of neutrophil membrane-camouflaged iron oxide particles in the diagnosis of stroke-induced neuroinflammation has not yet been reported.

Herein, we designed neutrophil-mimetic magnetic nanoprobes (NMNPs) with targetability to activated endothelial cells for enhanced neuroinflammation imaging (Fig. 1). The inner core of NMNPs is composed of poly(lactic-*co*-glycolic acid) (PLGA) nanoparticles loaded with superparamagnetic iron oxide (SPIO), which are FDA-approved polymer matrices and contrast agents.[25] The biomimetic outer shell of NMNPs is derived from the membranes of neutrophils, utilizing the naive biocompatibility and targetability of living neutrophils rather than their proinflammatory effect.[26] Furthermore, a rodent model of transient middle cerebral artery occlusion (tMCAO) is used to induce neuroinflammation and assess the diagnosis efficacy of NMNPs. The injected NMNPs can selectively target activated cerebral endothelial cells for enhanced neuroinflammation magnetic resonance imaging (MRI). Finally, NMNPs have superior application prospects from bench-to-bedside attributed to the biocompatibility of PLGA and the neutrophil membrane.

Results and discussion

Preparation and characterization of NMNPs

For proof of our idea, we first prepared NMNPs composed of a SPIO-loaded PLGA nanocore and a neutrophil membrane coating shell in the following three steps: (1) synthesis of SPIO and fabrication of magnetic PLGA nanoparticles (MNPs), (2) preparation of neutrophil membrane-derived vesicles (NVs), and (3) then coating of MNPs with NVs. SPIO and magnetic

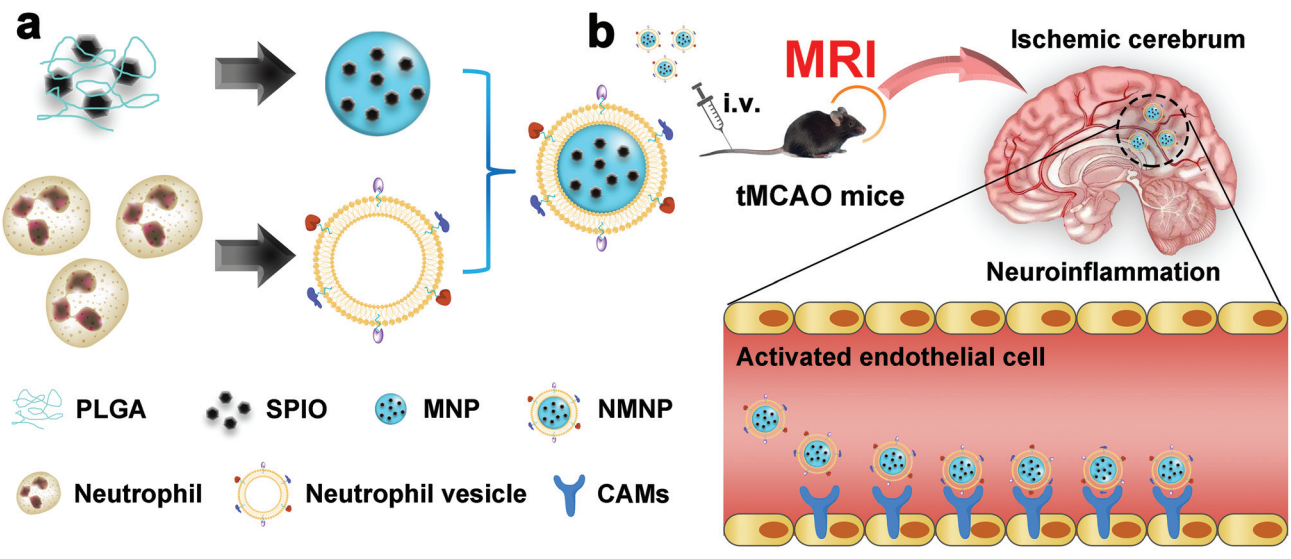

Fig. 1 Schematic illustration of neutrophil-mimetic magnetic nanoprobes (NMNPs) for enhanced stroke-induced neuroinflammation imaging by targeting the activated endothelial cells. (a) A diagram of the fabrication of NMNPs. Firstly, SPIO loaded PLGA nanoparticles (MNPs) were prepared using a simple emulsion solvent evaporation method. Secondly, neutrophil membrane-derived vesicles (NVs) along with the membrane proteins were collected from the neutrophils, which were isolated from mouse bone marrow. Thirdly, NVs were fused onto the surface of MNPs using a sonication process. (b) After intravenous injection, NMNPs could effectively bind to activated endothelial cells, attributing to the innate targeting ability inherited from neutrophils. The resulting enriched NMNPs were then used for enhanced *in vivo* neuroinflammation magnetic resonance imaging.

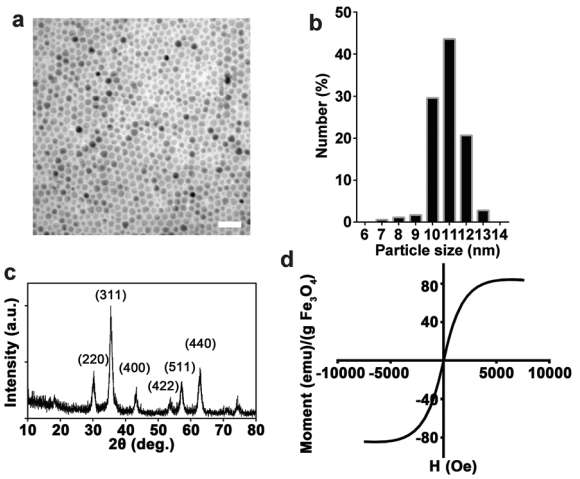

Fig. 2 Characterization of the synthesised SPIO. (a) TEM image, (b) the size distribution histograms, (c) X-ray diffraction pattern and (d) the room-temperature hysteresis loop of SPIO nanoparticles. Scale bar = 50 nm.

PLGA nanoparticles were prepared according to our previous report with slight modifications.[27] Briefly, the monodisperse nanocrystals of SPIO were synthesized using a high-temperature reductive decomposition method.[28] The transmission electron microscopy (TEM) image and the corresponding size-distribution histogram showed that the synthesised SPIO had a narrow size distribution, with an average particle size of 10.5 nm (Fig. 2a and b). The crystal information and magnetic properties of SPIO were confirmed using an X-ray diffractometer (XRD) and a vibrating sample magnetometer (Fig. 2c and d), respectively. The position and relative intensity of all diffraction peaks match well with the standard Fe_3O_4 peaks and the synthesized SPIO exhibited an excellent superparamagnetism, with a calculated magnetisation saturation of 83.8 emu g^{-1}. Next, PLGA nanoparticles containing SPIO (MNPs) were prepared using a simple emulsion solvent evaporation method.[29] Remarkably, the prepared MNPs showed an excellent stability; their particle size was almost unchanged for 6 months in aqueous solution upon storage at 4 °C (Fig. S1†).

The neutrophils were then isolated from mouse bone marrow according to our previous report,[26] followed by the subsequent hypotonic swelling and physical homogenization to obtain purified NVs. Next, a neutrophil membrane-coated nanoprobe (NMNPs) was prepared by fusing the purified NVs on the surface of magnetic PLGA nanoparticles using a sonication process.[30] Dynamic light scattering (DLS) measurements revealed that the resulting NMNPs had an average particle size of 159.9 nm, which was ~16 nm greater than the uncoated MNPs, and possessed an equivalent surface zeta potential to that of the NVs (Fig. 3a). Furthermore, the transmission electron microscopy (TEM) images showed a spherical core–shell structure of NMNPs, which displayed a unilamellar membrane over their magnetic polymeric cores (Fig. 3b; Fig. S2†). Moreover, evenly distributed SPIO were observed within both uncoated and coated spherical nanoparticles. All of these indicated a successful neutrophil membrane coating on the MNPs.

To quantify the content of SPIO, inductively coupled plasma atomic emission spectrometry (ICP-AES) was performed which indicated that 38.9 wt% and 28.6 wt% of SPIO were incorporated into MNPs and NMNPs, respectively (Table S1†). Accordingly, the weight percentage of the neutrophil membrane was calculated to be about 26.2% in NMNPs. From the ICP analysis, we found that NMNPs contained as much as ~30% SPIO, and the high loading efficiency may enhance the negative contrast in T_2-weighted MRI images.[29] To confirm the MRI contrast-enhancing effect of NMNPs, various nanoparticle dispersions were evaluated using a 7.0 T MRI system. The T_2-weighted relaxation rate value (R_2) of NMNPs was calculated to be 486.5 mM^{-1} s^{-1} (Fig. 3c), which was close to that of MNPs, suggesting that the neutrophil membrane coating does not affect the MRI functionality, and that NMNPs are suitable as a T_2 MRI contrast agent. To investigate the colloidal stability, the size change of NMNPs in 100% foetal bovine serum (FBS) was evaluated over time (Fig. 3d). Compared to MNPs, NMNPs showed improved colloidal stability, suggesting a protective effect of the neutrophil membrane coating. Collectively, we confirmed the successful fusion of neutrophil vesicles onto MNPs and provided evidence to support the excellent MRI functionality and colloidal stability of NMNPs.

Surface proteins on NMNPs

Accumulating evidence showed that the biocompatibility, immune-evasive ability and high binding affinity of neutrophils to activated endothelial cells were strongly linked to the various membrane proteins on the cell membranes.[22,24] To verify the reservation of membrane proteins on the surface of NMNPs, protein profiles were analysed by sodium dodecyl sulfate-polyacrylamide gel electrophoresis (SDS-PAGE) (Fig. 4a). Neutrophils and NVs were also prepared in parallel for comparison. It was found that the profile of proteins tracked on NMNPs was similar to that on the neutrophil membrane, reflecting successful translocation of the neutrophil membrane proteins to the surface of NMNPs. It is worth mentioning that NMNPs retained most of the neutrophil membrane proteins in a highly concentrated manner, mainly due to the enrichment effect when preparing NVs.

Meanwhile, the specific binding affinity of neutrophils to inflamed endothelial cells could be mainly attributed to the various adhesion molecules expressed on the surface of neutrophils, such as selectins and integrins. Among these proteins, several representative adhesion proteins including CD18, CD11a, CD11b, PSGL-1 and LFA-1 were examined, since they all play crucial roles during the neutrophil–endothelium interaction.[20,31] Western blot analysis revealed the presence of all these adhesion proteins on the surface of NMNPs (Fig. 4b).

Moreover, CD47 was also found on the surface of NMNPs, which could improve the immune-evading capabilities of the resulting nanocarriers.[32] To verify the anti-phagocytic capability of NMNPs, mouse macrophage RAW264.7 cells were incubated with rhodamine-labelled MNPs and NMNPs and

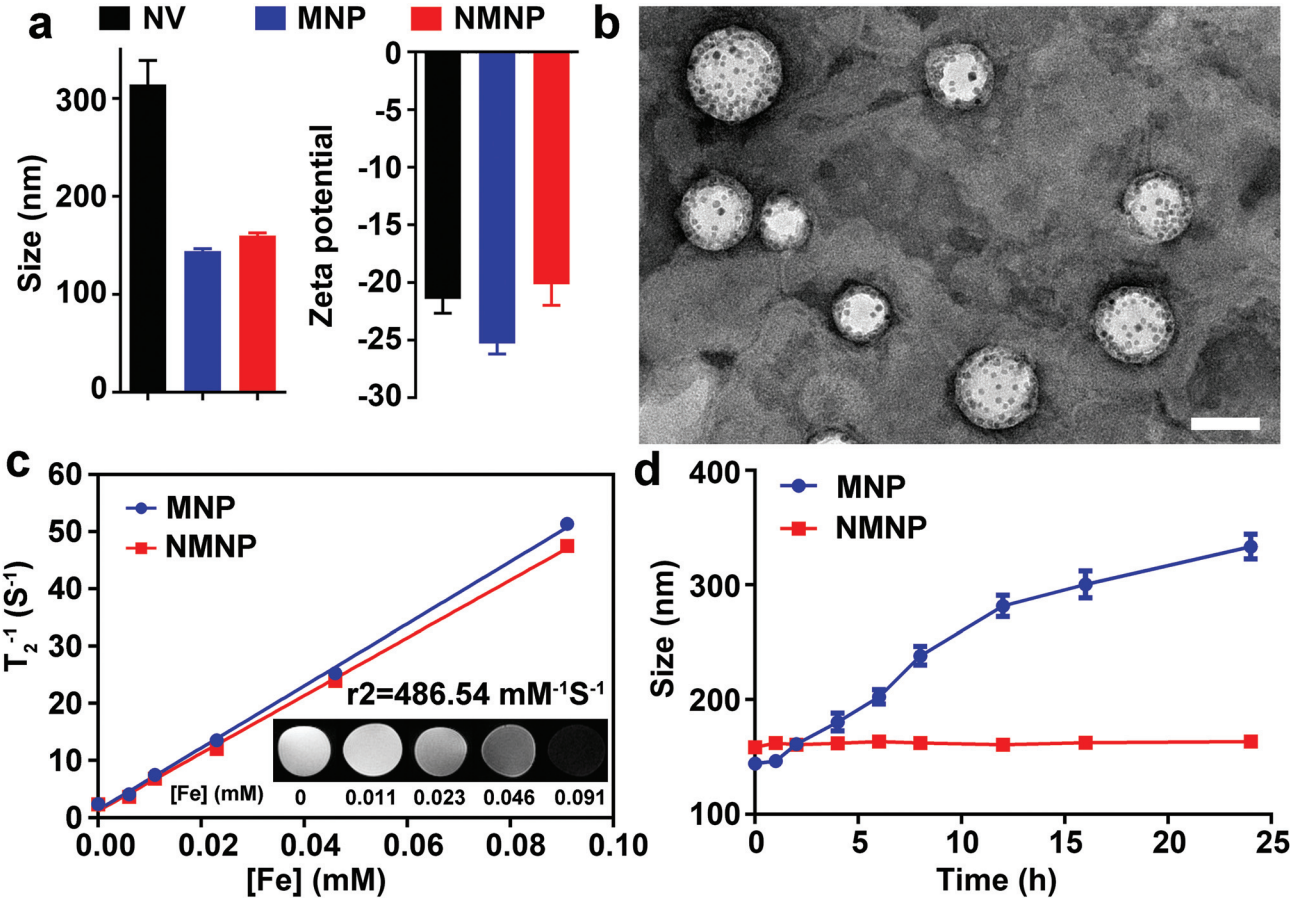

Fig. 3 Characterization of NMNPs. (a) Particle sizes and zeta potentials of the neutrophil vesicles, MNPs, and NMNPs, respectively. Error bars indicate SD (n = 3). (b) TEM images of NMNPs. Scale bar = 100 nm. (c) T_2 relaxation rate values (R_2) of MNPs and NMNPs at different iron concentrations. The inset shows the R_2 values of NMNPs and their T_2-weighted MRI images at different iron concentrations. (d) 100% FBS stability of MNPs and NMNPs monitored by dynamic light scattering at 37 °C. Error bars indicate SD (n = 3).

visualised using confocal laser scanning microscopy (CLSM) (Fig. S3†). As expected, NMNPs exhibited a significantly attenuated macrophage uptake, which was in accordance with quantitative analysis by ICP-AES (Fig. S4†). As a result, it is believed that the NMNPs could avoid immune phagocytosis and possess the potential to adhere to activated endothelial cells.

In vitro binding affinity to activated endothelium

To demonstrate the binding capability of NMNPs to activated endothelial cells *in vitro*, the intracellular uptake of NMNPs by human umbilical vein cells (HUVECs) was studied. First, a cell viability assay was performed, and the effects of NMNPs on HUVECs were negligible (Fig. S5†), further indicating the good biocompatibility of NMNPs. Subsequently, HUVECs were incubated with various rhodamine-labelled nanoprobes and visualised using CLSM (Fig. 4c). The HUVECs were pre-treated with tumor necrosis factor-α (TNF-α) to imitate activated endothelial cells with upregulation of ICAM-1 and E-selectin according to previous reports.[22,33] Meanwhile, red blood cell membrane-coated MNPs (RMNPs) were used as a negative control, which had similar physicochemical properties to NMNPs, except that they lacked specific adhesion molecules. It was observed that incubation of the NMNPs with activated HUVECs resulted in significantly increased uptake as compared to RMNPs or incubation of the NMNPs with non-activated HUVECs, suggesting that the interaction between NMNPs and HUVECs requires the adhesion molecules expressed on both neutrophils and the endothelium.

To quantitatively analyse the interaction, the iron contents in collected HUVECs were determined by ICP-AES (Fig. 4d). The iron contents in the NMNP group were about 3.0-fold higher than that in the non-activated HUVEC group, and 3.5-fold higher than that in the RMNP group, which exhibited a similar tendency to that observed in the confocal fluorescence images. These results indicate that coating of MNPs with a neutrophil membrane can preferentially increase their affinity to activated endothelial cells, attributing to the successful transfer of cell adhesion molecules with binding properties.

In vivo binding affinity to inflamed cerebral endothelium

Although there is evidence for a high affinity between NMNPs and activated endothelial cells, the *in vivo* targeting ability of

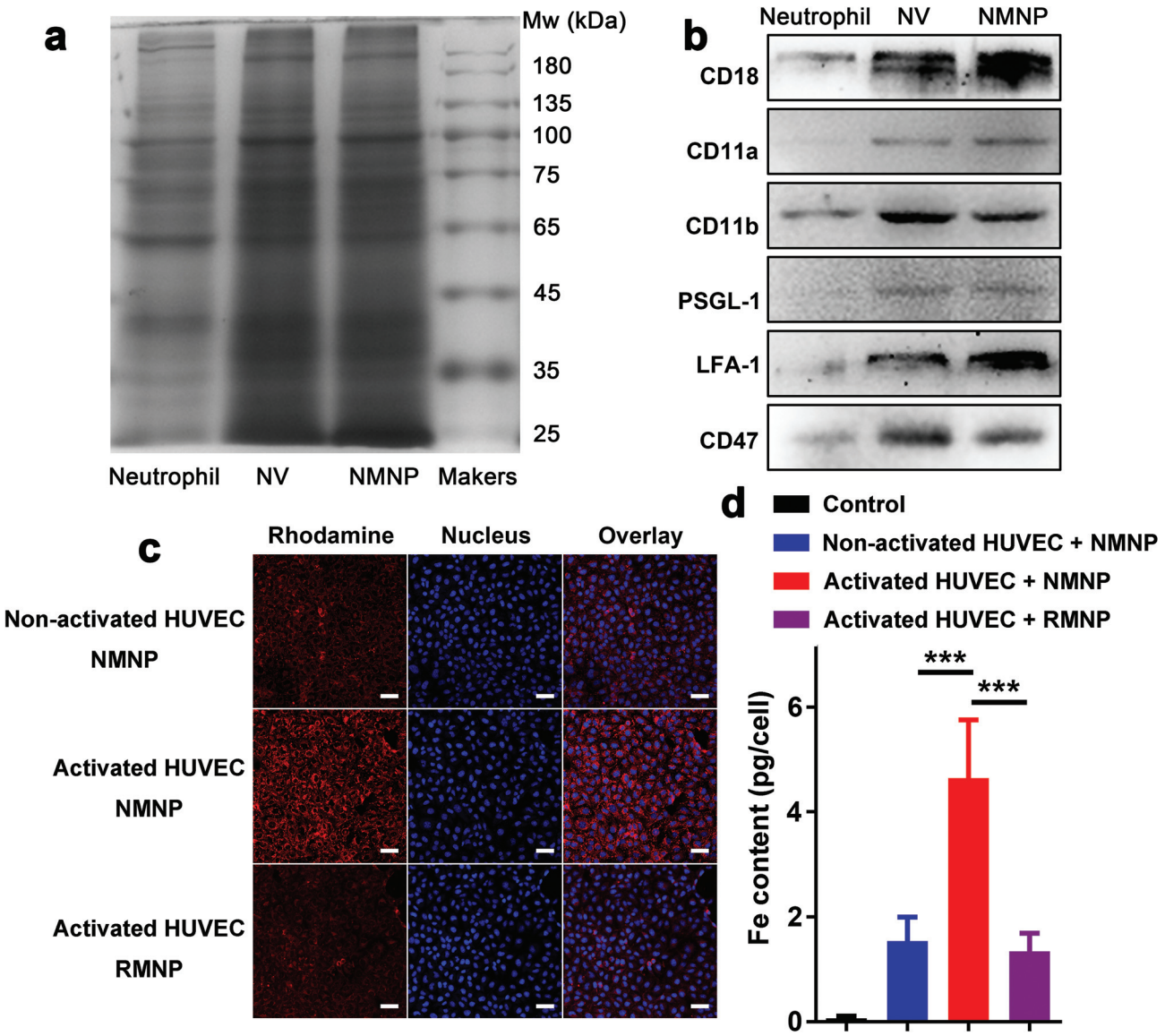

Fig. 4 *In vitro* studies on the binding of NMNPs to activated endothelium. (a) SDS-PAGE analysis of neutrophils, NVs and NMNPs. (b) Western blot of CD18, CD11a, CD11b, PSGL-1, LFA-1 and CD47 on neutrophils, NVs and NMNPs. (c) CLSM images of HUVECs after incubation with rhodamine-labelled MNPs and NMNPs (red). HUVECs were stained with DAPI (blue). Activated HUVECs were pre-stimulated with TNF-α, followed by incubation with NMNPs or RMNPs. The red blood cell membrane-coated MNPs (RMNPs) were used as a negative control. Scale bar = 50 μm. (d) Quantitative analysis of uptake of various nanoparticles by activated or normal HUVECs. Error bars indicate SD (n = 6). ***P < 0.001.

NMNPs to inflamed cerebral endothelial cells is inconclusive. To address whether NMNPs can target inflamed cerebral micro-vessels in ischemic stroke, we established a tMCAO mouse model to mimic stroke-induced neuroinflammation. First of all, we evaluated the brain distribution of NMNPs in the ischemic region using an *ex vivo* imaging system (Fig. 5a). *Ex vivo* fluorescence imaging of isolated brains indicated that NMNPs exhibited the highest fluorescence intensity in the ischemic region and the fluorescence intensity decreased a little over time, which could be due to the long-circulation and targetability of the neutrophil membrane coated on MNPs. Meanwhile, nonspecific retention of NMNPs was almost absent from the contralateral brain region. Quantification analysis revealed that the fluorescence intensity in the NMNP group was 4.8-fold higher than that in the MNP group, and 7.9-fold higher than that in the RMNP group (Fig. 5b). These results indicated that NMNPs could selectively accumulate in the damaged ischemic region.

Although we have shown that NMNPs accumulated in the ischemic region, it is not clear whether NMNPs could bind to inflamed cerebral endothelial cells. In order to visualize the *in vivo* nanoprobe–endothelium interactions, a cranial window for real-time visualization of nanovesicles in a live mouse brain was established. Rhodamine-MNPs were then injected to fluorescently labelled blood vessels. Subsequently, DiR-labelled NMNPs were administered intravenously into the

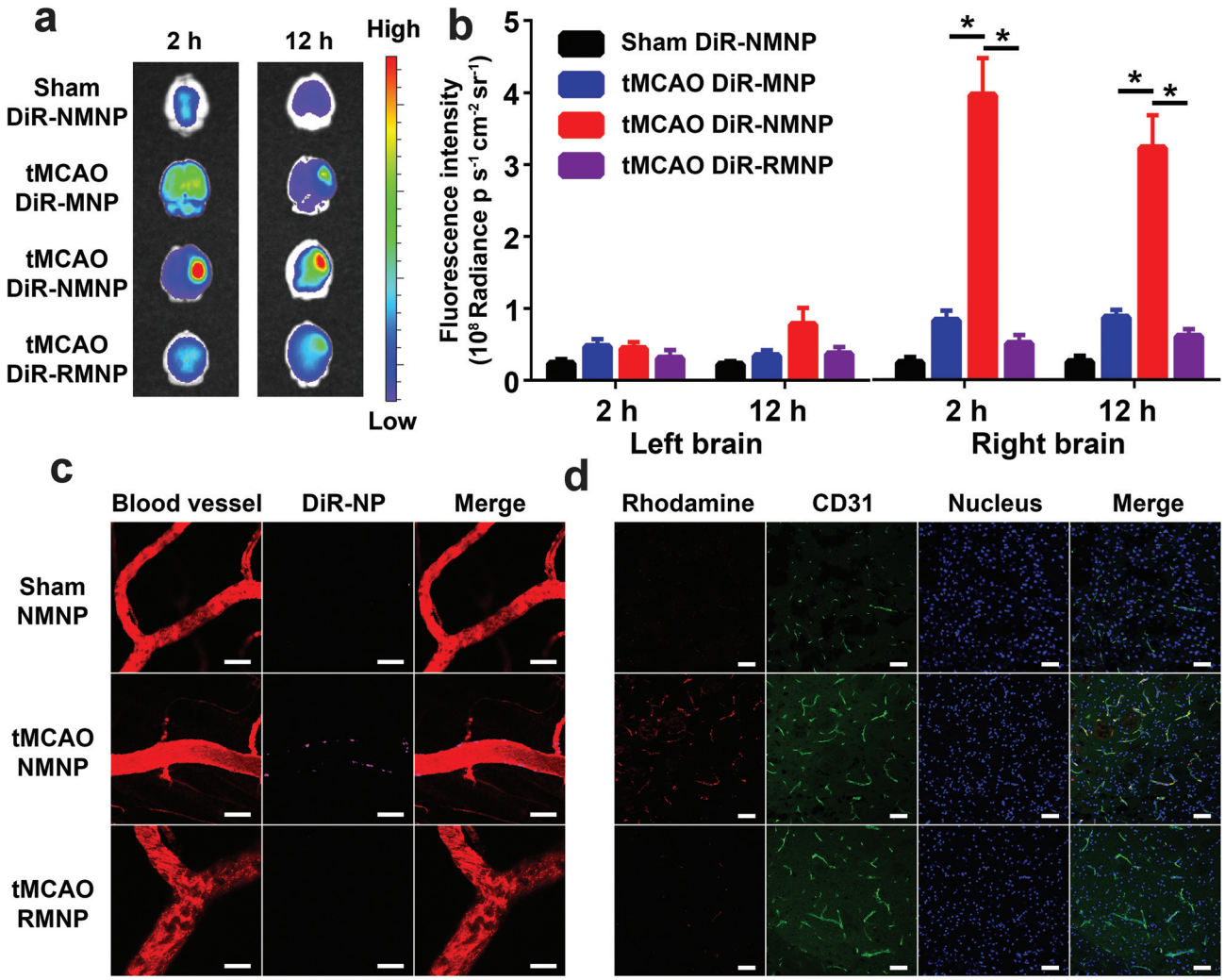

Fig. 5 Specific adhesion of NMNPs to inflamed cerebral endothelium *in vivo*. (a) *Ex vivo* fluorescence imaging of brains at 2 and 12 h after treatment with DiR-MNP, DiR-NMNP or DiR-RMNP in tMCAO mice, and DiR-NMNP in normal mice. (b) Quantification of the fluorescence intensity of region-of-interest brains. Error bars indicate SD (n = 3). *P < 0.05. (c) Intravital images of live mouse cerebral microvessels in tMCAO mice after intravenous infusion of DiR-NMNP or DiR-RMNP, and DiR-NMNP in normal mice. Rhodamine-MNPs were intravenously injected to label blood vessels (red). Scale bar = 50 μm. (d) Immunofluorescence image of brain sections from a tMCAO mouse treated with rhodamine-NMNP or rhodamine-RMNP (red), and rhodamine-NMNP in normal mice. Cerebral microvessels were stained with CD31 (green). Scale bar = 50 μm.

mouse. Using real-time imaging, the DiR-labelled NMNPs (purple) successfully adhered to the inflamed cerebral microvasculature (red), while we could not observe this phenomenon when DiR-RMNPs were administered (Fig. 5c). In addition, in the immunofluorescence images of brain sections, a higher CD31 (green) background was observed in the tMCAO group in comparison to the sham group due to the increased angiogenesis after tMCAO according to previous reports.[34,35] Notably, rhodamine-labelled NMNPs (red) and CD31-labelled cerebral microvasculature (green) colocalized perfectly in the ischemic region (Fig. 5d), which further verified the superior binding affinity of NMNPs to inflamed endothelium. Altogether, the results demonstrated that the neutrophil membrane coated magnetic nanoprobes could specifically target the inflamed cerebral microvasculature in the ischemic region, thus providing a tool for the diagnosis of stroke-induced neuroinflammation.

In vivo magnetic resonance imaging of stroke induced neuroinflammation

Vascular endothelial cell activation is a hallmark of stroke-induced neuroinflammation, and we have proved that the neutrophil membrane camouflaged magnetic nanoprobes could effectively bind to inflamed cerebral microvessels. To test and verify whether NMNPs can enhance the MRI contrast of stroke-induced neuroinflammation, we constructed a murine tMCAO model for *in vivo* studies. These model mice were intravenously administered with NMNPs or RMNPs 24 h after reperfusion, followed by MRI detection 2 h later (Fig. 6a). The sham-operated mice served as the negative controls. T_2^* weighted

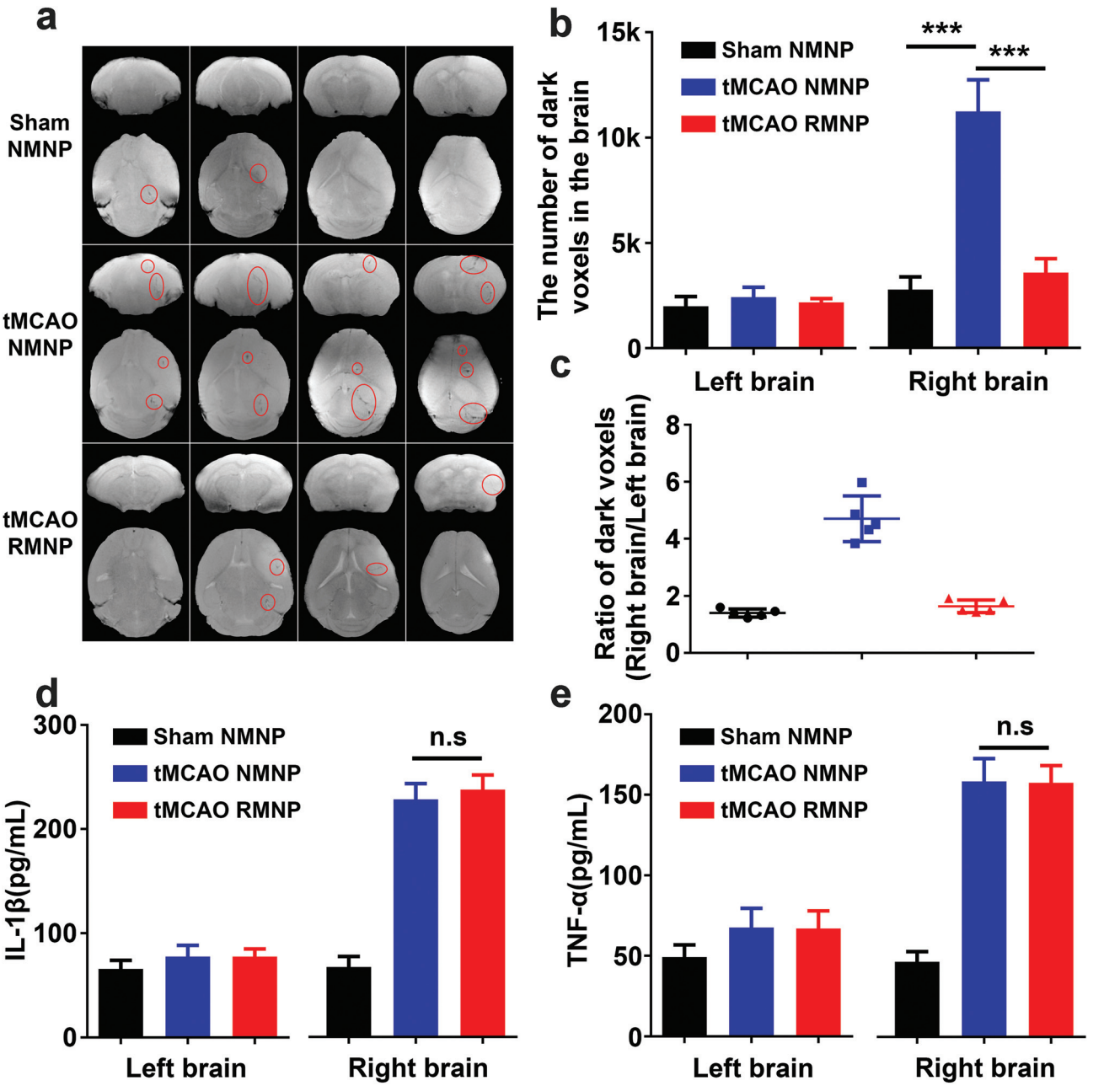

Fig. 6 *In vivo* magnetic resonance imaging of stroke-induced neuroinflammation. (a) T_2^* -Weighted coronal and transverse images at 2 h after injection of NMNPs and RMNPs, which was 26 h later after reperfusion. (b) The total number of dark voxels in the ipsilateral and contralateral region of the mice from groups NMNPs and RMNPs. Error bars indicate SD (n = 5). *P < 0.001. (c) The number of dark voxels in the ipsilateral ischemic region expressed as a ratio of the mirrored contralateral region. Error bars indicate SD (n = 5). (d and e) Expression levels of IL-1β (d) and TNF-α (e) in the left and right brains of tMCAO mice treated with NMNPs and RMNPs. Error bars indicate SD (n = 5). The sham-operated mice injected with NMNPs served as the negative controls.

sequences were chosen to identify the various magnetic nanoprobes as they are extremely sensitive to susceptibility effects. In contrast to the RMNP group, the mice treated with NMNPs caused a marked MRI contrast effect, which manifested as intensely low signal areas that appeared to delineate brain blood vessels on the ipsilateral side of ischemic brain tissue. Additionally, nonspecific retention was almost absent from the contralateral brain region, consistent with the *ex vivo* brain imaging result. Sham-operated mice that underwent the same injection regime with NMNPs showed a negligible contrast effect. The quantification analysis of the MRI contrast effect was further confirmed by calculating the total number of dark voxels in the ischemic region (Fig. 6b and c). There were significant differences between the various groups when the total number of dark voxels in the right brain (ischemic region) was compared. The largest number of dark voxels overall in the

right brain was observed in the NMNP treated mice and the ipsilateral signal was 4.0 times higher than that in the sham mice and 3.1 times higher than that in the RMNP treated mice. Moreover, the ratio of the ipsilateral *versus* contralateral signal was also significant in the NMNP treated mice. Finally, the levels of inflammatory factors, such as TNF-α and IL-1β, in the ipsilateral and contralateral regions were also determined to evaluate the degree of neuroinflammation (Fig. 6d and e), which was consistent with magnetic resonance imaging. In brief, activated vascular endothelial cells could be visualized using MRI after NMNP injection, suggesting the viability of NMNPs for diagnosing stroke-induced neuroinflammation.

In vivo biodistribution and biodegradability evaluation

In vivo biosafety is always a considerable concern for nanomaterials used in biomedicine. For preliminarily investigation of the biodistribution of NMNPs, Prussian blue staining was used to detect the biodistribution of iron introduced by NMNPs (Fig. 7a). The images showed that iron was mainly distributed in the luminal surfaces without extravasation, which is consistent with the previous intravital fluorescence and immunofluorescence images. These results provided further evidence that NMNPs selectively adhered to the inflamed vascular endothelial cells. However, it was no accident that most of the iron existed in the spleen and liver. Despite the fact that most of the NMNPs were transferred to the spleen and liver, they could be eliminated over time according to the quantitative analysis of the iron content in the treated mice brains by ICP-AES (Fig. 7b). Furthermore, no noticeable signal of liver and spleen damage was observed in the H&E staining sections (Fig. 7c). All these results suggested a good biocompatibility of these neutrophil membrane-coated magnetic nanoprobes, which have alluring prospects for clinical application.

Experimental

Cell lines

The mouse macrophage cell line RAW264.7 and the human umbilical vein endothelial cells were all purchased from the American Type Culture Collection.

Preparation and characterization of NMNPs

Synthesis and characterization of SPIO. Monodisperse SPIO nanoparticles were synthesized by a one-pot hydrothermal

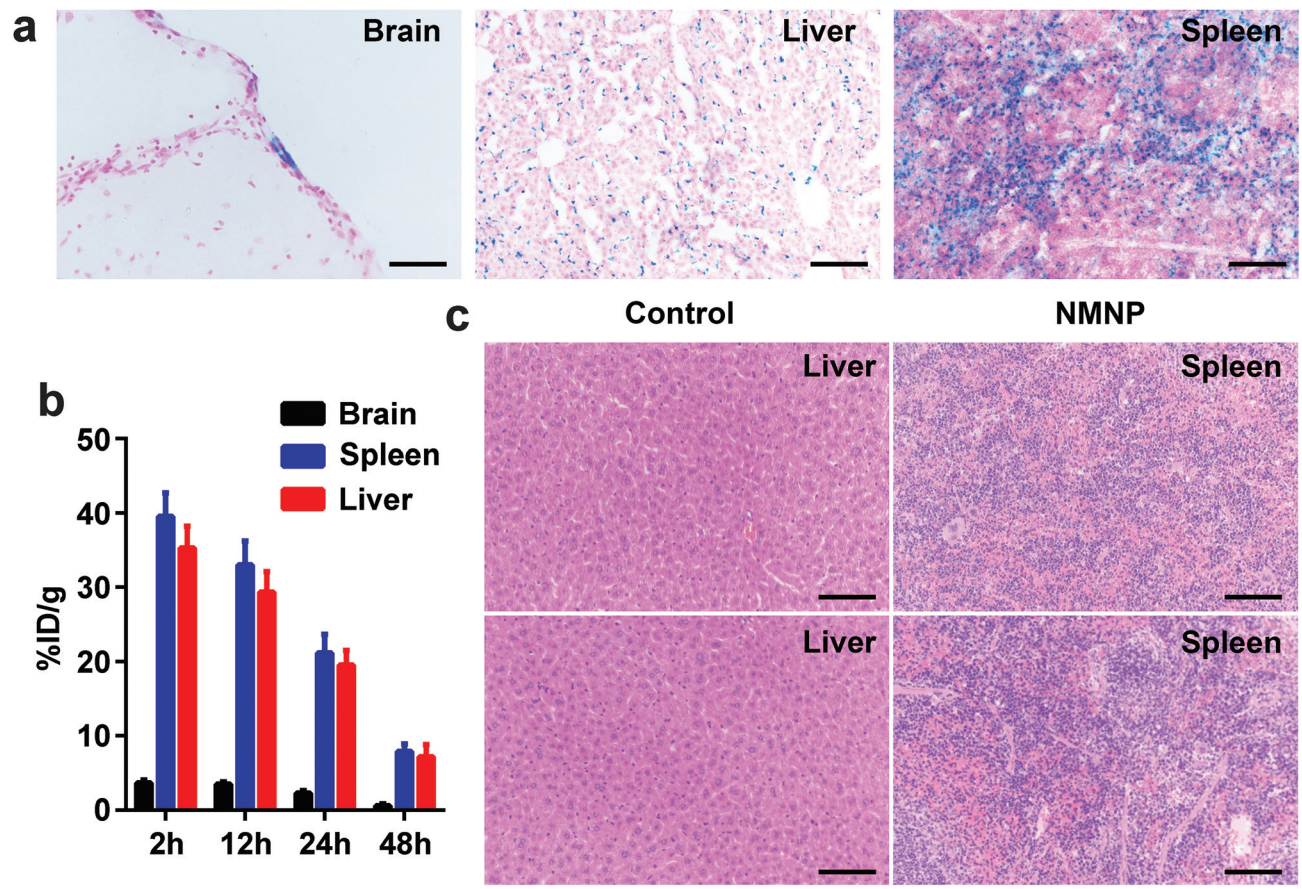

Fig. 7 *In vivo* biodistribution and biodegradability evaluation. (a) Prussian blue staining of ischemic brain, liver and spleen sections in tMCAO mice treated with NMNPs. Scale bar = 50 μm in the brain. Scale bar = 100 μm in the liver and spleen. (b) Quantitative analysis of the iron content in ischemic brain, liver and spleen at different time points after NMNP injection. Error bars indicate SD (n = 5). (c) Representative H&E staining slices of the liver and spleen. Scale bar = 100 μm.

method.[28] Briefly, 2 mmol $Fe(acac)_3$ was dissolved in a mixture of 10 ml of benzyl ether and 10 mL of oleylamine. The solution was dehydrated at 110 °C for 1 h and quickly heated to 300 °C and it was kept at this temperature for 2 h. 50 mL of ethanol was added to the solution after it was cooled to room temperature. The precipitate was collected by centrifugation at 4500 rpm and washed with ethanol thrice. The final product of SPIO nanoparticles was re-dispersed in dichloromethane for future use.

Samples for TEM were prepared by drying the obtained SPIO nanoparticle solutions on a copper grid and imaged by transmission electron microscopy (TEM, Hitachi H-7650) at 80 kV.

X-ray powder diffraction patterns of the obtained SPIO nanoparticles were obtained on a Bruker AXS D8-Advanced diffractometer with Cu Kα radiation (λ = 1.5418 Å).

Magnetic properties were studied using a Lakeshore 7300 high sensitivity vibrating sample magnetometer (VSM) with fields up to 1.5 tesla at room temperature.

Preparation of MNPs. PLGA nanoparticles containing SPIO nanocrystals were prepared using a modified conventional oil-in-water (O/W) single emulsion evaporation method.[29] Briefly, 10 mg of PLGA and a certain amount of SPIO nanocrystals were added to 1 mL of methylene chloride. This mixture was emulsified with 10 mL of the PVA aqueous solution (1 wt%) using a probe type sonicator at 100 w for 5 min in an ice bath. The resulting suspension was stirred for 6 h at room temperature to evaporate the organic solvent and subsequently centrifuged at 13 000 rpm for 30 min. The obtained MNPs were washed three times with distilled water and resuspended in water. The DiR and rhodamine labelled PLGA nanoparticles were prepared by a similar method to that described above except for using 0.1 wt% DiR instead of SPIO nanocrystals or PLGA-rhodamine instead of PLGA-COOH.

Preparation of NVs. In order to prepare neutrophil membrane-cloaked MNPs, mature neutrophils were isolated from murine bone marrow using a modified method.[36] Briefly, the femur and the tibia from both hind legs were immersed in RPMI 1640 medium after removal of the muscle and sinew. The bone marrow was flushed from the bone with HBSS-EDTA solution, centrifuged at 200*g* for 3 min and resuspended in 1 mL of HBSS-EDTA. The cells were laid on a Percoll mixture solution consisting of 55%, 65% and 75% Percoll followed by centrifugation at 1500*g* for 30 min. The mature neutrophils were recovered at the interface of the 65% and 75% fractions and washed with ice-cold HBSS-EDTA thrice. The obtained neutrophils were treated with 10 μM fMLF (Sigma, St Louis) for 10 minutes at 37 °C, washed with ice-cold HBSS-EDTA thrice, and stored at −80 °C for subsequent membrane derivation.

The neutrophil membrane was derived by a hypotonic swelling method.[23] Briefly, frozen neutrophils were thawed, pelleted by centrifugation at 1000*g* for 3 min, and washed with ice-cold 1× PBS thrice. Neutrophils were then suspended in hypotonic lysing buffer containing 30 mM Tris-HCl (pH 7.5), 225 mM D-mannitol, 75 mM sucrose, and a proteinase inhibitor cocktail. Neutrophils were then disrupted using a Dounce homogenizer with a tight-fitting pestle (20 passes). The homogenized solution was centrifuged at 20 000*g* for 30 min at 4 °C. The pellet was discarded and the supernatant was centrifuged again at 100 000*g* for 40 min at 4 °C. After the centrifugation, neutrophil membranes were collected as the pellet and washed twice with 1× PBS containing proteinase inhibitor cocktail. The obtained neutrophil membranes were suspended in water and sonicated in a capped glass vial for 3 min using a bath sonicator to obtain NVs.

Preparation of NMNPs. Finally, neutrophil membrane cloaking was accomplished by dispersing and fusing NVs with MNP nanoparticles by sonication using a bath sonicator for another 5 min.

Characterization of NMNPs. The particle size and surface zeta potential of NVs, MNPs and NMNPs were characterized using DLS, respectively. The morphologies were determined by transmission electron microscopy (TEM, JEM-200CX, JEOL, Japan). The samples were prepared by allowing the nanoparticle droplets at a concentration of 100 μg mL^{-1} to come in contact with copper grids for 5 min, removing the excess droplets, and staining using 1% uranyl acetate for 30 s before the TEM studies. The loading efficiency of SPIO nanocrystals was quantified by ICP-AES (Optima 5300DV, PE, USA).

The MRI capability of MNPs and NMNPs was evaluated using a 7.0 T whole body MRI system (Biospec 7T/20 USR, Bruker, Germany). T_2-Weighted MRI images of MNPs and NMNPs at a series of Fe concentrations were acquired for T_2 relaxation rate (r_2) assessment.

The *in vitro* stability of MNPs and NMNPs was evaluated by measuring their diameters in 100% FBS for 24 h using DLS.

Coomassie blue staining and western blotting analysis were employed to identify the proteins on neutrophils, NVs and NMNPs. Briefly, the samples containing equivalent total proteins measured using a BCA protein assay kit (Life Technologies) were added to 10% SDS-polyacrylamide gel to separate different molecular weights of proteins. Subsequently, the resulting polyacrylamide gel was stained with Coomassie blue and imaged. The key membrane proteins were identified by western blotting using primary antibodies including anti-CD47 (absin, China), anti-CD18 (Abcam, Cambridge, MA), anti-CD11a (Abcam, Cambridge, MA), anti-CD11b (absin, China), anti-PSGL-1 (4RA10, BioXcell) and anti-LFA-1 (absin, China).

In vitro immune escape evaluation

RAW 264.7 cells (1×10^5 cells per dish or well) were seeded in confocal dishes and 6-well plates and cultured for 24 h. Then the cells were incubated with rhodamine-labeled MNPs and NMNPs for 4 h. Thereafter, the cells in confocal dishes were washed with PBS three times, stained with Hoechst 33342, fixed with 4% PFA and imaged by CLSM (LSM 880, Zeiss). To quantify the Fe uptake by RAW 264.7 cells, the cells in 6-well plates were lysed by adding 0.5 mL 1% Tween 80 to each well. The cell lysate from each well was then added to 1 mL of nitric acid. The mixture samples were left at room temperature for

12 h, followed by annealing at 80 °C for 6 h to remove the acid, and finally resuspended in DI water for Fe content determination by ICP-AES (Optima 5300DV, PE, USA).

In vitro cytotoxicity assay and HUVEC binding affinity

For the *in vitro* cytotoxicity assay, HUVEC cells (1×10^4 cells per well) were seeded in 96-well plates and cultured for 24 h. Then the cells were pre-treated with 10 ng mL^{-1} TNF-α (R&D Systems, Minneapolis, MN) for 4 h. Afterward, HUVECs were incubated with different concentrations (*i.e.*, 12.5, 25, 50, 100, 200, 400 and 800 μg ml^{-1}) of MNPs and NMNPs for 12 h, followed by adding 5 mg mL^{-1} CCK-8 solution. After 4 h of incubation, the absorbance was measured at a wavelength of 450 nm using a microplate reader. Cells grown without any treatment were used as a control.

For the HUVEC binding affinity assay, HUVEC cells (1×10^5 cells per dish or well) were seeded in confocal dishes and 6-well plates and cultured for 24 h. Then the cells were pre-treated with or without 10 ng mL^{-1} TNF-α for 4 h at 37 °C. Afterward, HUVECs were incubated with 100 μg ml^{-1} of rhodamine-labelled NMNPs and RMNPs for 2 h. Thereafter, the cells in confocal dishes were washed with PBS three times, stained with Hoechst 33342, fixed with 4% PFA and imaged by CLSM (LSM 880, Zeiss). To quantify the Fe uptake by HUVEC cells, the cells in 6-well plates were lysed by adding 0.5 mL 1% Tween 80 to each well. The cell lysate from each well was then added to 1 mL of nitric acid. The mixture samples were left at room temperature for 12 h, followed by annealing at 80 °C for 6 h to remove the acid, and finally resuspended in DI water for the Fe content determination by ICP-AES (Optima 5300DV, PE, USA).

Mouse transient middle cerebral artery occlusion (tMCAO) model

The mouse transient middle cerebral artery occlusion (tMCAO) model was prepared using a modified intraluminal filament technique.[37] C57BL/6 mice (male, 6–8 weeks old) were purchased from the Comparative Medicine Center of Yangzhou University. All the animal experiments were performed in compliance with the Guide for Care and Use of Laboratory Animals approved by China Pharmaceutical University.

Briefly, the right common carotid artery (CCA), external carotid artery (ECA) and internal carotid artery (ICA) were carefully dissected and exposed through midline neck incision. MCA occlusion was performed by introducing a silicon-coated 6–0 monofilament suture (Doccol Corporation) into the CCA through ECA and advancing it 9 ± 1 mm *via* ICA to the origin of MCA. Reperfusion was initiated by withdrawing the filament after 1 h. Apart from the sham group, all other groups underwent MCAO/reperfusion surgery. All experiments were performed and quantified in a randomized fashion by investigators blinded to treatment groups.

Ex vivo brain imaging and quantification of NMNPs in the ischemic region

Male C57BL/6 mice with ischemic stroke were used for *ex vivo* brain imaging. DiR-loaded MNPs, NMNPs and RMNPs at a DiR dose of 20 nmol kg^{-1} were intravenously injected at 24 h post-reperfusion of the MCAO model. Meanwhile, DiR-loaded NMNPs injected in the sham group were set as the negative control. 2 h and 12 h after injection, the mice were sacrificed. The brain tissues were dissected for *ex vivo* fluorescence imaging using an *in vivo* imaging system (PerkinElmer, USA). The fluorescence intensities of the regions-of-interest (ROI) were analysed using Living Image Software.

Real-time fluorescence intravital microscopy

In vivo intravital microscopy of mouse brain vasculature was performed as reported.[38] The cranial window was first placed on the mouse right brain. At least 7 days after the operation, MCAO was performed on the mouse with a cranial window. Ischemia was operated on the right artery to induce the injury in the right brain. One hour later, the mouse was reperfused after the filament in the artery was withdrawn. DiR-labelled NMNPs and RMNPs were administered 4 h after reperfusion. 15 minutes later, RhB-PLGA was i.v. injected to label bloodstream, and circulation and binding of NMNPs or RMNPs were observed using a ×20/1.0 NA water immersion objective lens and a high-speed camera (Zeiss LSM 880, Germany). A healthy mouse (without I/R) was used as the control. During imaging, all mice were placed on a thermo-controlled blanket at 37 °C on an intravital microscope tray and under anesthesia with 1.5% isoflurane.

Immunofluorescence staining

RhB-loaded NMNPs and RMNPs were intravenously administered to tMCAO mice 24 h after reperfusion. Approximately 2 h later, the mice were sacrificed. The brains were removed without perfusion and fixed in 4% formaldehyde for 4 h, followed by dehydration in 15% sucrose and then in 30% sucrose. Brains were frozen with O.C.T at −80 °C and coronal series sections (30 μm) were cut on a freezing microtome (Leica CM1520, Germany). Sections were blocked with 10% goat serum at room temperature for 1 h and then incubated with anti-CD31 antibody (Servicebio, China) at 4 °C overnight. After washing, brain sections were incubated with the secondary antibody Alexa Flour™ 488 (Thermo Fisher Scientific, San Jose, CA) for 1 h. Brain sections were examined using a confocal microscope (LSM 880, Zeiss, Germany). A healthy mouse (without I/R) was used as the control.

Inflammatory cytokine measurement

For TNF-α and IL-1β measurement, infarcted and non-infarcted half brains were collected and homogenized. The supernatant was collected and analysed for TNF-α and IL-1β levels using the corresponding ELISA kits. Experiments were conducted according to the protocol in triplicate.

Prussian blue staining

NMNPs were intravenously administered to tMCAO mice 24 h after reperfusion. Approximately 2 h later, the mice were sacrificed. The brain, liver and spleen were removed without perfusion and fixed in 4% formaldehyde for 4 h, followed by de-

hydration in 15% sucrose and then in 30% sucrose. Brains were frozen with O.C.T at −80 °C and coronal series sections (20 μm) were cut on a freezing microtome (Leica CM1520, Germany). Prussian blue staining was performed using a Prussian blue iron stain kit (Servicebio, China). All sections were examined using an inverted fluorescence microscope (Ts2R, Nikon, Japan).

In vivo magnetic resonance imaging of stroke induced neuroinflammation

To study the MRI of activated endothelial cells in ischemic stroke, 200 μL of NMNPs and RMNPs (10 mg iron per kg, $n = 5$ per group) were intravenously injected 24 h after reperfusion. A healthy mouse (without I/R) was used as the control. 2 h after NMNP or RMNP injection, the mice were placed in a quadrature birdcage coil with an in-built stereotaxic frame for imaging on a 7.0 T whole body MRI system (Biospec 7T/20 USR, Bruker, Germany). The imaging protocol consisted of T_2 measurement using a TurboRARE sequence (TR/TE: 2500/33 ms, flip angle 180°), and a fast low angle shot (FLASH) T_2^*-weighted sequence (TR/TE: 400/6.0 ms, flip angle 30°). For each magnetic resonance image, we manually masked the brain to exclude extracerebral structures. ImageJ freeware was used to segment and to quantify the number of dark voxels in the ischemic region.

Statistical analysis

All the data were presented as mean ± SD. Student's *t*-test was used for comparison between two groups, and the differences among multiple groups were analyzed by one-way ANOVA. The statistical significance was set at $^*P < 0.05$, and the extreme significance was set at $^{**}P < 0.01$ (GraphPad Prism 8.0.1).

Conclusions

In summary, inspired by the neutrophil–endothelium interaction in inflammatory response, we have developed a neutrophil membrane-cloaked magnetic nanoprobe that specifically targets inflamed cerebral endothelial cells and diagnoses stroke-induced neuroinflammation with high sensitivity. Compared to the traditional monoclonal antibody conjugation approach, the neutrophil membrane coating strategy endows magnetic nanoprobes with some special properties, such as biocompatibility, better targeting abilities and immunogenicity exemption. Although there are excellent advantages over this strategy, the source of neutrophils may limit its transformation to clinical applications. More work should be done to overcome this limitation, such as increasing the iron content of MNPs or increasing the utilization rate of neutrophil membranes. Overall, magnetic nanoprobes coated with a neutrophil membrane provide a safe and effective tool for diagnosing stroke-induced neuroinflammation and also offer potential application in treating other inflammatory disorders due to the ubiquitous neutrophil–endothelium interaction in the course of many diseases.

Author contributions

C.M.T.: Methodology, validation, writing – original draft. Q.Q.W.: Investigation, writing – review & editing. K.M.L.: Conceptualization, methodology, validation. X.Q.L.: Software, methodology. C.W.: Formal analysis & methodology. L.J.X.: Writing – review & editing. C.Y.J.: Conceptualization, supervision, methodology, writing – review & editing, funding acquisition. C.Z.: Supervision, funding acquisition, project administration.

Conflicts of interest

There are no conflicts to declare.

Acknowledgements

This work was supported by the National Natural Science Foundation of China (81930099, 81773664, 81473153, 82073785), the National Major Scientific and Technological Special Project for "Significant New Drugs Development" (2019ZX09301163), the 111 Project from the Ministry of Education of China and the State Administration of Foreign Expert Affairs of China (No. 111-2-07, B17047), the Open Project of State Key Laboratory of Natural Medicines (No. SKLNMZZ202017), the Natural Science Foundation of Jiangsu Province (BK20190558) and the "Double First-Class" University project (CPU2018GY47, CPU2018GF10).

References

1 E. J. Benjamin, S. S. Virani, C. W. Callaway, A. M. Chamberlain, A. R. Chang, S. Cheng, S. E. Chiuve, M. Cushman, F. N. Delling, R. Deo, S. D. de Ferranti, J. F. Ferguson, M. Fornage, C. Gillespie, C. R. Isasi, M. C. Jimenez, L. C. Jordan, S. E. Judd, D. Lackland, J. H. Lichtman, L. Lisabeth, S. Liu, C. T. Longenecker, P. L. Lutsey, J. S. Mackey, D. B. Matchar, K. Matsushita, M. E. Mussolino, K. Nasir, M. O'Flaherty, L. P. Palaniappan, A. Pandey, D. K. Pandey, M. J. Reeves, M. D. Ritchey, C. J. Rodriguez, G. A. Roth, W. D. Rosamond, U. K. A. Sampson, G. M. Satou, S. H. Shah, N. L. Spartano, D. L. Tirschwell, C. W. Tsao, J. H. Voeks, J. Z. Willey, J. T. Wilkins, J. H. Wu, H. M. Alger, S. S. Wong, P. Muntner, E. American Heart Association Council on, C. Prevention Statistics and S. Stroke Statistics, *Circulation*, 2018, **137**, e67–e492.

2 G. A. Donnan, M. Fisher, M. Macleod and S. M. Davis, *Lancet*, 2008, **371**, 1612–1623.

3 P. M. George and G. K. Steinberg, *Neuron*, 2015, **87**, 297–309.

4 R. L. Jayaraj, S. Azimullah, R. Beiram, F. Y. Jalal and G. A. Rosenberg, *J. Neuroinflammation*, 2019, **16**, 142.

5 M. A. Moskowitz, E. H. Lo and C. Iadecola, *Neuron*, 2010, **67**, 181–198.

6 L. H. Deddens, G. A. Van Tilborg, W. J. Mulder, H. E. De Vries and R. M. Dijkhuizen, *Cerebrovasc. Dis.*, 2012, **33**, 392–402.
7 M. Gauberti, A. Montagne, A. Quenault and D. Vivien, *Front. Cell. Neurosci.*, 2014, **8**, 389.
8 B. Zinnhardt, M. Wiesmann, L. Honold, C. Barca, M. Schafers, A. J. Kiliaan and A. H. Jacobs, *Theranostics*, 2018, **8**, 2603–2620.
9 H. L. Lutsep, G. W. Albers, A. DeCrespigny, G. N. Kamat, M. P. Marks and M. E. Moseley, *Ann. Neurol.*, 1997, **41**, 574–580.
10 A. Neuwelt, N. Sidhu, C. A. Hu, G. Mlady, S. C. Eberhardt and L. O. Sillerud, *AJR, Am. J. Roentgenol.*, 2015, **204**, W302–W313.
11 S. Warach, J. F. Dashe and R. R. Edelman, *J. Cereb. Blood Flow Metab.*, 1996, **16**, 53–59.
12 U. Dirnagl, C. Iadecola and M. A. Moskowitz, *Trends Neurosci.*, 1999, **22**, 391–397.
13 M. S. Kluger, *Adv. Dermatol.*, 2004, **20**, 163–201.
14 M. Thakur and B. C. Lentle, *AJR, Am. J. Roentgenol.*, 2006, **186**, 297–299.
15 A. M. Chacko, E. D. Hood, B. J. Zern and V. R. Muzykantov, *Curr. Opin. Colloid Interface Sci.*, 2011, **16**, 215–227.
16 M. Gauberti, A. P. Fournier, F. Docagne, D. Vivien and S. Martinez de Lizarrondo, *Theranostics*, 2018, **8**, 1195–1212.
17 L. C. Hoyte, K. J. Brooks, S. Nagel, A. Akhtar, R. Chen, S. Mardiguian, M. A. McAteer, D. C. Anthony, R. P. Choudhury, A. M. Buchan and N. R. Sibson, *J. Cereb. Blood Flow Metab.*, 2010, **30**, 1178–1187.
18 M. A. McAteer, N. R. Sibson, C. von Zur Muhlen, J. E. Schneider, A. S. Lowe, N. Warrick, K. M. Channon, D. C. Anthony and R. P. Choudhury, *Nat. Med.*, 2007, **13**, 1253–1258.
19 A. Tsourkas, V. R. Shinde-Patil, K. A. Kelly, P. Patel, A. Wolley, J. R. Allport and R. Weissleder, *Bioconjugate Chem.*, 2005, **16**, 576–581.
20 L. Yang, R. M. Froio, T. E. Sciuto, A. M. Dvorak, R. Alon and F. W. Luscinskas, *Blood*, 2005, **106**, 584–592.
21 G. C. Jickling, D. Liu, B. P. Ander, B. Stamova, X. Zhan and F. R. Sharp, *J. Cereb. Blood Flow Metab.*, 2015, **35**, 888–901.
22 T. Kang, Q. Zhu, D. Wei, J. Feng, J. Yao, T. Jiang, Q. Song, X. Wei, H. Chen, X. Gao and J. Chen, *ACS Nano*, 2017, **11**, 1397–1411.
23 Q. Zhang, D. Dehaini, Y. Zhang, J. Zhou, X. Chen, L. Zhang, R. H. Fang, W. Gao and L. Zhang, *Nat. Nanotechnol.*, 2018, **13**, 1182–1190.
24 X. Dong, J. Gao, C. Y. Zhang, C. Hayworth, M. Frank and Z. Wang, *ACS Nano*, 2019, **13**, 1272–1283.
25 J. A. Frank, H. Zywicke, E. K. Jordan, J. Mitchell, B. K. Lewis, B. Miller, L. H. Bryant Jr. and J. W. Bulte, *Acad. Radiol.*, 2002, **9**(Suppl 2), S484–S487.
26 J. Xue, Z. Zhao, L. Zhang, L. Xue, S. Shen, Y. Wen, Z. Wei, L. Wang, L. Kong, H. Sun, Q. Ping, R. Mo and C. Zhang, *Nat. Nanotechnol.*, 2017, **12**, 692–700.
27 C. Tang, C. Wang, Y. Zhang, L. Xue, Y. Li, C. Ju and C. Zhang, *Nano Lett.*, 2019, **19**, 4470–4477.
28 V. Mazumder and S. Sun, *J. Am. Chem. Soc.*, 2009, **131**, 4588–4589.
29 J. Kim, S. Park, J. E. Lee, S. M. Jin, J. H. Lee, I. S. Lee, I. Yang, J. S. Kim, S. K. Kim, M. H. Cho and T. Hyeon, *Angew. Chem., Int. Ed.*, 2006, **45**, 7754–7758.
30 C. M. Hu, R. H. Fang, K. C. Wang, B. T. Luk, S. Thamphiwatana, D. Dehaini, P. Nguyen, P. Angsantikul, C. H. Wen, A. V. Kroll, C. Carpenter, M. Ramesh, V. Qu, S. H. Patel, J. Zhu, W. Shi, F. M. Hofman, T. C. Chen, W. Gao, K. Zhang, S. Chien and L. Zhang, *Nature*, 2015, **526**, 118–121.
31 C. E. Green, U. Y. Schaff, M. R. Sarantos, A. F. Lum, D. E. Staunton and S. I. Simon, *Blood*, 2006, **107**, 2101–2111.
32 C. Grimsley and K. S. Ravichandran, *Trends Cell Biol.*, 2003, **13**, 648–656.
33 K. Zen, D. Q. Liu, Y. L. Guo, C. Wang, J. Shan, M. Fang, C. Y. Zhang and Y. Liu, *PLoS One*, 2008, **3**, e1826.
34 M. Chen, W. Zou, M. Chen, L. Cao, J. Ding, W. Xiao and G. Hu, *Eur. J. Pharmacol.*, 2018, **833**, 221–229.
35 Q. Hu, L. Liu, L. Zhou, H. Lu, J. Wang, X. Chen and Q. Wang, *Exp. Neurol.*, 2020, **329**, 113312.
36 M. Swamydas and M. S. Lionakis, *J. Visualized Exp.*, 2013, e50586, DOI: 10.3791/50586.
37 E. Rousselet, J. Kriz and N. G. Seidah, *J. Visualized Exp.*, 2012, **69**, 4038.
38 H. Wang, L. J. Hong, J. Y. Huang, Q. Jiang, R. R. Tao, C. Tan, N. N. Lu, C. K. Wang, M. M. Ahmed, Y. M. Lu, Z. R. Liu, W. X. Shi, E. Y. Lai, C. S. Wilcox and F. Han, *Cell Res.*, 2015, **25**, 674–690.

